Micro and Nanostructures 195 (2024) 207957

Contents lists available at ScienceDirect

Micro and Nanostructures

journal homepage: www.journals.elsevier.com/micro-and-nanostructures

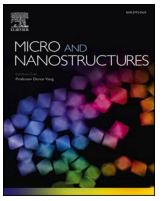

A strategy to predict the current conduction mechanisms into Al/PVP:Gr-$BaTiO_3$/p-Si Schottky structure using Artificial Neural Network

Yashar Azizian-Kalandaragh [a,b,c,**], Süleyman Özçelik [a,b], Ali Barkhordari [d,*], Şemsettin Altındal [e]

[a] Department of Photonics, Faculty of Applied Sciences, Gazi University, 06500, Ankara, Turkey
[b] Photonics Application and Research Center, Gazi University, 06500, Ankara, Turkey
[c] Department of Physics, University of Mohaghegh Ardabili, P.O. Box.179, Ardabil, Iran
[d] Faculty of Physics, Shahid Bahonar University of Kerman, Kerman, Iran
[e] Department of Physics, Faculty of Sciences, Gazi University, Ankara, Turkey

ARTICLE INFO

Keywords:
Schottky structures
Graphene/$BaTiO_3$ nanoparticles
Current conduction mechanisms
Electronic specifications
Artificial neural network (ANN)

ABSTRACT

In this work, Artificial Neural Network (ANN) algorithm is used to predict the current conduction mechanisms into the metal-semiconductor (MS) and metal-nanocomposite-semiconductor (MPS) structures along with their primary electronic parameters, such as the leak current (I_0), potential barrier height (Φ_{B0}), ideality factor (n), series/shunt resistance (R_s/R_{sh}), rectifying ratio (RR), and interface states density (N_{ss}) by analyzing the I–V characteristics. The polyvinylpyrrolidone (PVP), barium titanate ($BaTiO_3$) and graphene (Gr) nanoparticles are mixed together to create the interfacial nanocomposite layer. Training data for ANN algorithm is gathered using the thermionic emission hypothesis. In order to study the efficacy of the ANN model, the predictive power of the ANN technique for predicting the current conduction mechanisms and electronic properties of SDs has been assessed by comparing the predicted and experimental results. The ANN predictions of the current conduction mechanisms at the forward/reverse bias and the fundamental electronic specifications of the MS and MPS structures are a high level of agreement with the experimental results. Furthermore, the results show that the RR and R_{sh} rise whereas the n, R_s, and N_{ss} for MS structure decrease when the PVP:Gr-$BaTiO_3$ nanocomposite interlayer is employed.

1. Introduction

Based on the height value of the potential barrier, a metal-semiconductor (MS) configuration or Schottky diode (SD) in absence/presence an interlayer has been categorized as a rectifier or non-rectifier instrument [1]. The junction is able to be either ohmic or Schottky if the quantity of BH is low or high adequately [2–5]. To Schottky and Mott hypothesis [1,4,5], the front metal rectifying junctions, the semiconductor's work functions, and the rear metal ohmic also affect the ohmic and rectification response of these instruments.

* Corresponding author.
** Corresponding author. Department of Photonics, Faculty of Applied Sciences, Gazi University, 06500, Ankara, Turkey.
E-mail addresses: yasharazizian@gazi.edu.tr (Y. Azizian-Kalandaragh), alibarkhordari20@yahoo.com (A. Barkhordari).

https://doi.org/10.1016/j.micrna.2024.207957
Received 6 May 2024; Received in revised form 1 August 2024; Accepted 19 August 2024
Available online 20 August 2024

Whether semiconductor devices have a polymer interlayer or not, they need these structures, including transistors, capacitors, solar cells, and SD [3]. Increasing the performance and producing MS structures economically requires carefully selecting large-dielectric materials and metal/metal-oxide dopants in conjunction with a range of interfacial polymer/organic layers [3–7]. This presents the primary scientific and technological challenge confronting MS structures.

Today, the main scientific problems of metal-semiconductor (MS) structures are related to improving the performance of them and reducing their cost-production by developing some new interlayer-materials grown simple/easy grown technique such as hydro-thermal, electro-spinning, sol-gel, etc. [6–8]. Therefore, in the last two decades, some researchers have tried a lot of attempts to enhance the performance of MS structure by replacing polymers instead of conventional SiO_2 or SnO_2 insulators grown by traditional techniques [9]. Polymers are cheap, flexible and simple with high mechanical and dynamic strength to construct although they often have poor conductivity and dielectric constant. It is also useful to mention that polyvinyl alcohol (PVA) and polyvinyl pyrrolidone (PVP) can easy soluble in alcohol, simplifying the preparing process. Nevertheless, both the conductivity and dielectric values can be quite increased by doping some a suitable ratio of metallic and metal oxide elements like Zn, Gr, ZnO, Ba and St based high dielectric ferro-electric materials such as BTO and STO [8–10].

Furthermore, it needs to remember that the common insulator layers, which were made with outdated methods and positioned amidst semiconductor and metallic layers, were unable to minimize the leakage current and passivate the dangling bonds activated on the semiconductor surface [6–11].

Enhancements in the optical, electric, and dielectric specifications of the MS instruments featuring a polymer/organic interlayer without or with dopant of graphene, metallic, and metal oxide elements can also be ascribed to elements such as suitable mechanical and dielectric stability, large charge/energy storage capacity, simple processing manners, small weight, and adequate flexibility [12–15]. Therefore, potential BH has to be managed and regulated in order to enhance the MS structure's performance.

The electronic response of semiconductor devices (SDs) is dependent on the operating condition and influences their application in electronics technology. Furthermore, because sensitive laboratory testing is required, characterizing the electric characteristics of SDs is a time-consuming and expensive process. Therefore, very reliable engineering methodologies are required to predict the electrical properties of SDs. Nevertheless, there are often large deviations from the ideal situation from the theoretical and empirically observed electrical properties using thermionic emission theory.

These disparities are frequently caused by the series resistance (R_s), the interface states/traps (D_{it}/N_{ss}) formed at the semiconductor/interlayer interface, the inhomogeneity of the BH, the interlayer established nonuniformly between the M/S layers, and others. Therefore, it makes sense to employ alternative methods that can reduce the quantity of tests carried out, thereby conserving resources like time and money. At the moment, the most widely used method for accomplishing this objective is machine learning (ML). Studies have shown that ML is relevant in most scientific and technical disciplines and has been effective in the realm of Schottky configurations and the prediction of certain of their electronic characteristics.

ML is a branch of artificial intelligence that may grow a simulation model to anticipate new data by analyzing data samples and creating rules and patterns. It is a powerful, incredibly accurate prediction technology that replaces human judgement and middlemen in many industries. ML employs a wide range of modelling techniques to train the rules and then anticipate new data [13,14]. Recent research show that ML has been applied to many scientific and technical difficulties, including those in basic sciences (physics and chemistry), medical field (medicine and biology), computer vision, technology, and even finance [15–18]. Also, ML technique has been applied to the analysis of the electrical characteristics of SDs in the literature recently.

Torun et al. [19] investigated the I–V characteristics of Au/Ni/n-GaN SD at a temperature range from 40 K to 400 K using four machine learning algorithms. Adaptive Neuro Fuzzy System (ANFS), Gaussian Process Regression (GPR), Support Vector Regression (SVR), and Artificial Neural Network (ANN) were the approaches used to model the samples with 5192 experimental data. After gathering the error values of the model, they compared the models' efficacy and found that, of all the models employed, the AFNS algorithm performed the best throughout both phases, i.e., the train and test.

Ali et al. [20] estimated the electronic current of SDs in terms of temperature and voltage using an ANN according to the experimental data. They showed how the experimental data and the I–V values that the ANN model anticipated agreed well and with a respectable degree of accuracy. Using an ANN approach, Güzel et al. [21] represented the electronic current anticipation of 6H–SiC/MEH-PPV SDs with a polymer interlayer as a function of temperature and voltage applied. The experimental findings were recorded within the following temperature and voltage ranges: 100–250 K and -3V to +3V, respectively. The ANN algorithm's high accuracy and average variation of 0.15 % mean that the anticipated results agree with the experimental ones.

An interfacial layer that forms between metal and semiconductor can be thought of as a $BaTiO_3$ nanocomposite for applications in solar cells, capacitors, and MIS-type SDs [22–25]. As an interface layer amidst the Aluminum and p-silicon layers, barium titanate nano-powders are doped into the PVP in this study to enhance the electrical performance of the MS-type SD. Two SDs with the architectures of Al/p-Si (MS) and Al/PVP:Gr-$BaTiO_3$/p-Si (MPS) have been manufactured to examine their effects on the primary electronic characteristics of the MS-type SD. A brief description of the processes used to prepare the materials and create the SDs has been provided. Then, using the ML technique's Artificial Neural Network (ANN) algorithm, the electronic current of the SDs is predicted. In addition, their current conduction mechanisms (CCMs) will be determined and anticipated. Next, the main electric parameters, such as I_0, n, BH, R_s, R_{sh}, and RR, could then be computed and analyzed thanks to the application of the TE technique to the SDs' I–V characteristics of the manufactured SDs. By contrasting the predicted and actual results, the efficacy of the ML approach has been evaluated for accurately predicting the CCMs into SDs and their electrical properties.

2. Experimental procedures

2.1. Materials & devices

The precursors for the creation of the barium titanate ($BaTiO_3$) nanoparticles and Al/PVP:$BaTiO_3$/p-Si SD were titanium tetrachloride ($TiCl_4$), barium carbonate ($BaCO_3$), and sodium hydroxide (NaOH) produced by German company (Merck). The microwave was produced by a Korean company (Samsung) and has a frequency of 2450 MHz and a power range of 100–800 W. Polyvinyl pyrrolidine (PVP) polymer and p-type silicon wafer were used in the spin coater procedure to form the Al/PVP:Gr-$BaTiO_3$/p-Si SD. Moreover, the solutions of methanol (CH_3OH), ethanol (C_2H_5OH), hydrogen peroxide (H_2O_2), acetone (CH_3COCH_3), and hydrofluoric acid (HF) have been used to rinse the silicon wafers. To survey the surface morphology and optical characterization of the $BaTiO_3$ nano-powders, a scanning electron microscope (SEM) (Model: LEO 1430 VP) and UV–Vis spectrometer (Model: Shimadzu UV-1800) were applied, respectively. Additionally, the current-voltage characteristic (I–V) of the produced SDs at room temperature was examined by KEITHLEY (Model 2450).

2.2. Preparation of $BaTiO_3$ nano-powder & SD

In order to synthesize barium titanium, a 20^{cc} solution comprising 0.2 M of precursors for titanium dioxide (TiO_2), sodium hydroxide (NaOH), and barium carbonate ($BaCO_3$) was provided in 3 beakers individually by accounting for the stoichiometric proportions of the processes. At this point, the bismuth nitrate ($Ba(NO_3)_3$) solution was supplemented dropwise with solutions of titanium dioxide (TiO_2) and sodium hydroxide (NaOH) using ultrasonic irradiation. The solution's pH was 13 throughout this phase. After that, the solution was subjected to an 800 W microwave radiation exposure for 10 min. After a 5-min rinse with deionized water, the yellow mixture was allowed to dry at room temperature. After the solid powder was generated, the water molecules were removed by heating it to 700 °C for 2 h, resulting in the formation of a barium titanate nano-powder. Fig. 1 represents the providing steps of the $BaTiO_3$ nano-powder schematically.

For preparing the Si wafer surface for overlaying the polymer layer and forming a MPS SD, the surface must be cleaned of contaminants and the intrinsic silicon dioxide layer must be removed. It is therefore necessary to wash the Si wafer in a variety of solvents. The silicon wafer in this study was washed three times: once using a combination of CH_3COCH_3 and CH_3OH for 5 min at 55 °C; once using a mixture of NH_4OH, H_2O, and H_2O_2 for 15 min at 70 °C. The last step involves utilizing a solution of water H_2O and HF for 2 min at room temperature.

On a p-Si wafer, a crystal at the plane of (100) with a resistance of 1–10 Ω cm^{-1} and a thickness of 300 μm, the Al/PVP: BaTiO3 structure is deposited. Using the sputtering approach, an aluminum coating of 100 nm in thickness was sprayed at a pressure of 1 μTorr on the silicon wafer's bottom in order to provide the proper ohmic contact. Then, the layer was annealed at 500 °C. After creating a 5 % PVP solution by solvating 5 g of PVP nano-powders in 95^{cc} of distilled water, 10 mg of $BaTiO_3$ along with 5 mg of graphene were dispersed using an ultrasonic method to create the PVP:Gr-$BaTiO_3$ nanocomposite. Furthermore, a thin layer of the PVP:Gr-$BaTiO_3$ nanocomposite, measuring 100 nm in thickness, was created on the behind side of the Si wafer using the spin coater process with 3000 rpm at 1 min. Finally, the ohmic contacts were deposited in circular form onto the PVP:Gr-$BaTiO_3$ nanocomposite layer using Al masks with a 1.2 mm diameter and 100 nm thickness. As a result, two SDs were made employing the MS contact of Al/p-Si and the MPS

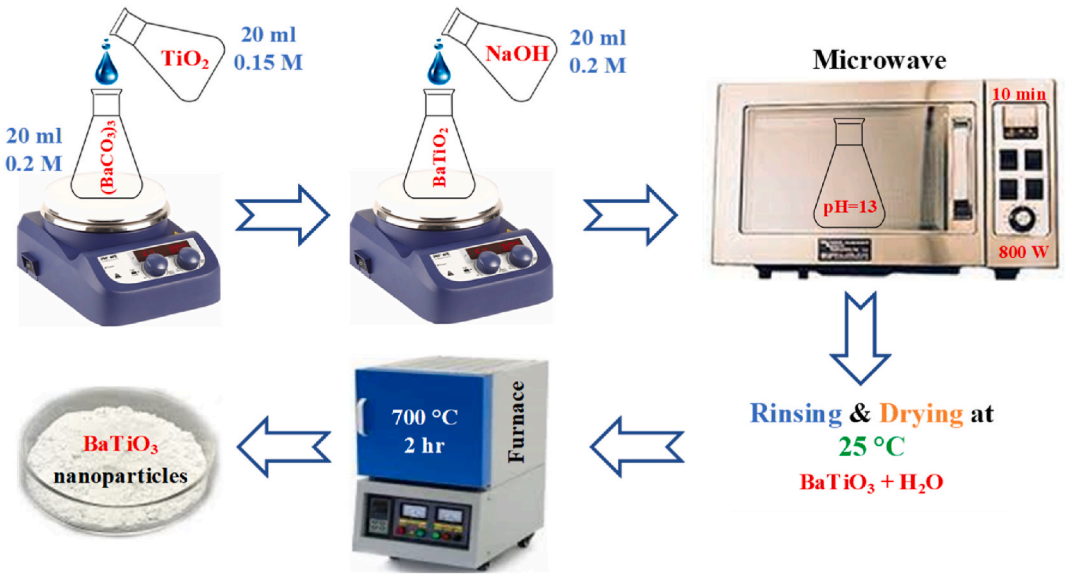

Fig. 1. Providing steps of $BaTiO_3$ nanostructures.

contact of Al/PVP:Gr-$BaTiO_3$/p-Si. It should be mentioned that a quartz thickness meter was applied for measuring the thickness of the ohmic and rectifier metal contacts, as well as the thickness of the interfacial layer was measured by the cross-section of the SEM images. A schematic of the produced SD with the PVP:Gr-$BaTiO_3$ interlayer is shown in Fig. 2.

3. ML algorithms

This study models the I–V characteristics and predicts the CCMs into Schottky devices as well as their various electronic characteristics using a machine learning technique, i.e., ANN. The results of the ANN algorithm are then compared with the experimental data. Below is a brief description of the ANN algorithm used in this work.

3.1. ANN algorithm

Backpropagation is a supervised learning approach used by a multilayer perceptron (MLP) to train the network. This technique enables the network to train from its mistakes and modify its parameters accordingly. Fig. 6 presents the schematic procedure followed in the ANN algorithm. Every node in an MLP, with the exception of the input nodes, is a linked layer of neurons with a nonlinear activation function [26]. A directed graph connects these nodes to construct a potent neural network. Neurons in two neighboring layers of an MLP are joined as a pair by the weighted edges. An input layer, one or more hidden layers, and an output layer are the minimum number of layers that make up an MLP.

The MLP can learn and produce predictions thanks to the connections between these layers, which provide information to go from the input data to the output results [27]. The output, y, is produced by the perceptron by passing a linear combination of weighted real-valued inputs via a nonlinear activation function, as shown in Ref. [26]:

$$y = \varphi\left(\sum_{i=1}^{n} w_i x_i + b\right) \tag{1}$$

where the bias, activation function, input and weights vectors are denoted by the letters b, φ, x and w, in that order. The functions of hyperbolic tangent, logistic sigmoid, and ReLU are frequently chosen by the MLP algorithms as the activation functions [28]. To reduce the output error, the MLP modifies the weights of the hidden layers. The error function might be expressed as follows by taking into account the difference between the desired (T_n) and actual ($O_n(t)$) values: [26];

$$E(O_n(t)) = T_n - O_n(t) \tag{2}$$

Actually, the primary goal of the training process is to minimize the error function. The step sizes at which weights are modified can be decreased and the convergence rate can be altered by using a learning parameter η (<1). To update the ith weight associated with the jth output, the subsequent rule is applied [26]:

$$w_{ij}(t+1) - w_{ij}(t) = \eta E\big(O_j(t)\big) \tag{3}$$

An iterative weight adaption process is shown in Equations (1)–(3), where the weight from the current iteration (t) is added to a portion of the output error from the following iteration (t + 1). Supervised-learning pattern recognition tasks are widely used MLPs. The spectacular successes of deep learning have rekindled interest in MLP backpropagation networks [29]. This study uses 20 hidden layers, each with 70 neurons, to create MLP with an activation function of ReLU. Electric current is present in the output layer, whilst applied voltage and absence/presence interfacial layer make up the input layer.

3.2. Errors functions and accuracy

As stated before, after the ML model construction is complete, a comprehensive analysis of prediction competency is needed. Furthermore, the computation and subsequent examination of the performance characteristics let us understand the prediction accuracy. Accordingly, the following parameters-mean absolute error (MAE) and mean squared error (MSE)-specify the correctness of the ML model, i.e., ANN, used in this work [30]:

$$MAE = \frac{1}{N}\sum_{i=1}^{N}\left|X_{\exp\,(i)} - X_{ANN(i)}\right| \tag{4}$$

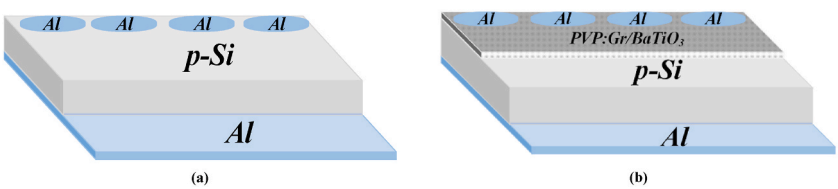

Fig. 2. Schematic of the produced (a) MS and (b) MPS samples.

$$MSE = \frac{1}{N}\sum_{i=1}^{N}\left(X_{\exp(i)} - X_{ANN(i)}\right)^2 \tag{5}$$

Among the other measures that show how correct the algorithm is the R2 score. The model's training and hyperparameter selection inside the method are generally better when the R2 score is closer to one, producing predictions with a reduced mean square error (MSE). If the R2 score quantity is zero, which would indicate that the hyperparameters have not been chosen well, the model would inappropriately perform on an unknown dataset. A model is said to be perfect when its R2 score is one. The calculation is as follows [31]:

$$R2\ \text{Score} = 1 - \frac{\sum_{i=1}^{N}\left(X_{ANN(i)} - X_{\exp(i)}\right)^2}{\sum_{i=1}^{N}\left(\overline{X}_{\exp\ (i)} - X_{\exp\ (i)}\right)^2} \tag{6}$$

Where, in turn, X_{ANN}, X_{exp}, and $\overline{X}_{exp}$ stand for the predicted value of the ANN model, the experiment value (actual value), and the mean quantity of experiment data. Table 1 shows the MAE value of the ANN method that was taken into consideration and utilized to anticipate the current value of SDs in absence/presence of interlayer. The MAE values have been evaluated with respect to 1.

It is evident that, in predicting the electronic current of considered SDs, the MAE value for the MPS-type SD in the ANN model is less than that of the MS-type SD. This situation could also be seen in the MSE and RMSE values for the fabricated SDs. Additionally, the R2 score values of the ANN algorithm for both SDs are near to unity, indicating that they did a good job managing the prediction (see Table 1). The MPS SD has an R2 score for electronic current prediction that is somewhat greater than the MS SD's.

4. Results and discussion

4.1. Absorbance & transmittance of the $BaTiO_3$ nanostructures

Using UV–Vis absorption spectroscopy, the optical characteristics of the $BaTiO_3$ nanostructure are investigated. Fig. 3 shows the UV–Vis absorbance and transmittance spectra of the $BaTiO_3$ nanostructure in the wavelength range of 200–800 nm. It is evident that the absorbance of the $BaTiO_3$ nanostructure intensively decreases by the growing the wavelength up while the transmittance increase.

Yet, the following formula, known as the Tauk equation, is used to determine the optical band gap:

$$\alpha h\upsilon = C\left(h\upsilon - E_g\right)^m \tag{7}$$

The coefficient of absorbance (α), photon energy (hυ), a constant (C), and band gap energy (E_g) are all represented in this equation [32]. Moreover, m can have two values for the direct and indirect transitions, 0.5 and 2. On the other hand, when $(\alpha h\upsilon)^2 = 0$, the linear component is extended to the energy axis, meaning that the intercept point lines up with the E_g. Fig. 4 shows the profile of $(\alpha h\upsilon)^2$ as a function of photon energy (hυ) with a tangential line determining the band gap energy (E_g). It should be mentioned that the computed band gap energy of 2.30 eV has a high level of agreement with the value found in the literatures [33].

4.2. Field emission-scanning electron microscopy (FE-SEM) images

The morphology of the produced $BaTiO_3$ nanostructures has been examined using FE-SEM images that were obtained using the microwave technique. Fig. 5 shows the surface morphological images of the produced $BaTiO_3$ nanoparticles as evaluated by the SEM test. Although actual particle sizes are hard to observe, a variety of shaped, agglomerated, and polydispersity nanoparticles might be created. With a mean size of around 70 nm and an average cluster size of <1 μm, each nanoparticle is shown to have a unique form.

4.3. I–V measurements and ANN prediction

Using experimental data at ±6 V, and ANN at ±1 V, Fig. 7 illustrates the I–V characteristics of the produced SDs without/with PVP: Gr-$BaTiO_3$ nanocomposite interlayer. It must be mentioned that the total number of I–V data was 482 in this work, the data was divided into three sets: train set (70 %), test set (20 %), and validation set (10 %). Note that the test set could be arbitrarily tuned at each part of the voltage range and hence, the ANN algorithm can be used to predict the fabricated diodes' main electronic parameters and CCMs. In order to predict the electronic parameters, the test set was selected in such a way that the predicted value in the range of −1 to 1 V.

Table 1
The errors and accuracy values of the ANN algorithm in predicting the electronic current for both SDs.

ANN Mod / SD	MAE	MSE	RMSE	R2_Score
MS	0.0731	0.0155	0.1245	0.9897
MPS	0.0314	0.0059	0.0766	0.9889

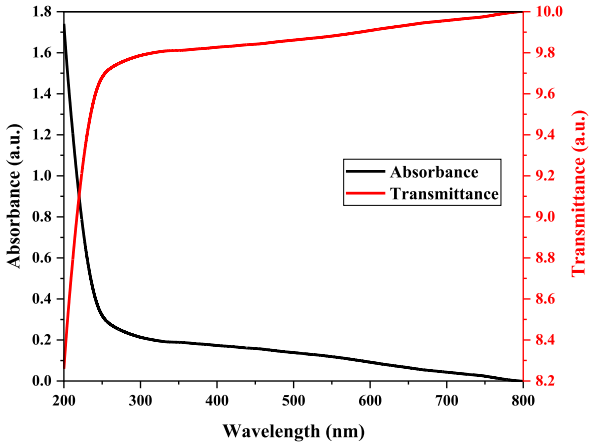

Fig. 3. The absorbance and transmittance spectra of the $BaTiO_3$ nanostructures.

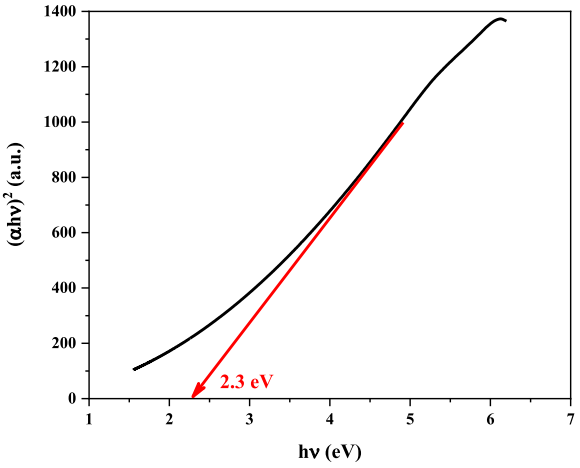

Fig. 4. The plot of $(\alpha h\upsilon)^2$-hυ of the $BaTiO_3$ nano-powder and it's the band gap energy.

Furthermore, as the ML approach requires a very large amount of data in order to effectively anticipate the new data, as opposed to other approaches like Norde and Cheung, the TE theory is utilized to examine the I–V characteristics of the created SDs. It's important to note that the TE hypothesis relies on the need that the BH be significantly larger than kT, which means that only electrons with sufficient energy to cross the potential barrier are considered for determining the current density. On the other hand, it is supposed that the plane controlling emission has reached thermal equilibrium and that an existence of a net current flow has no effect on the equilibrium [34]. It is evident that the ANN model predicts the electronic current of the MPS SD at various biases well rather than the MS SD and validates their error values (see Table 1).

To contrast the prediction accuracy of the ANN model, Fig. 8 concurrently shows the anticipated and real amounts for each SD with and without a nanocomposite interlayer. The experimental and output data locations are shown by the x- and y-axes, in that order. To offer a more comprehensive understanding of prediction precision, data point placements need to be approximated. The zero-error line was constructed in Fig. 8 specifically to help study the data points' locations more closely. The location of the data points for the ANN algorithm in relation to the zero-error line is another sign that the model can accurately predict the electrical current.

4.4. ANN prediction of CCMs at forward and reverse bias regions

Additionally, the influence of the absence/presence of an interlayer on the electronic current of free carriers are compared between the SDs, and the CCM in both the forward and reverse bias regions of the SDs is examined. It must be noted that the voltage location of the test data could be changed to predict the electronic current at the different voltage regions for additional analysis. The $Ln(I_F)$-V_F graphs of the MPS and MS SDs are shown in Fig. 9 at three distinct areas owing to various CCMs. In general, deep traps that develop at the interface and influence the I–V characteristics can be used to optimize charge transfer.

The slopes of the three distinct areas at the $Ln(I_F)$-V_F diagrams of the MS and MPS SDs are introduced in Table 2. The amounts of the

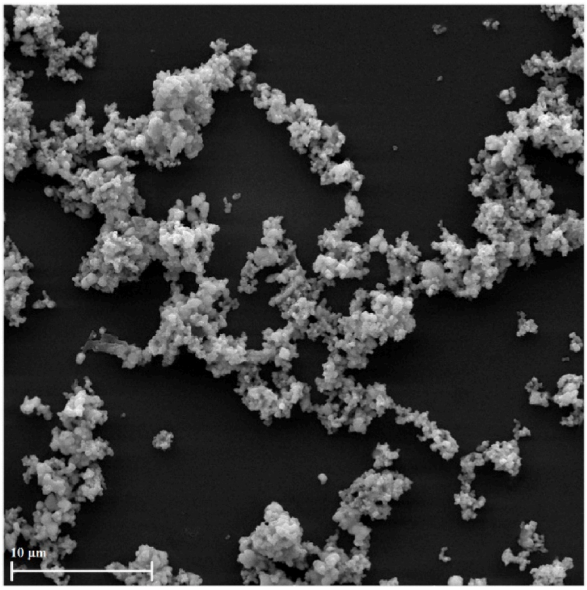

Fig. 5. FE-SEM illustration of the generated $BaTiO_3$ nanoparticles.

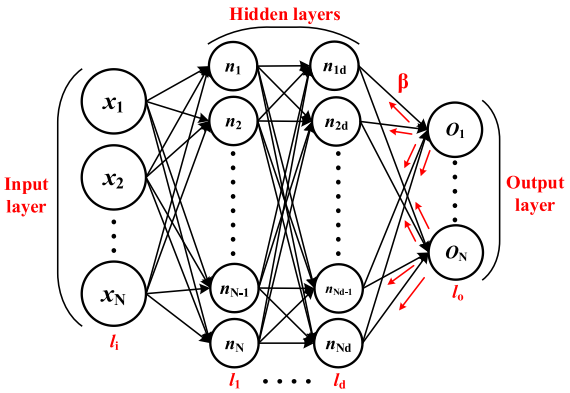

Fig. 6. Schematic procedure used in the ANN algorithm.

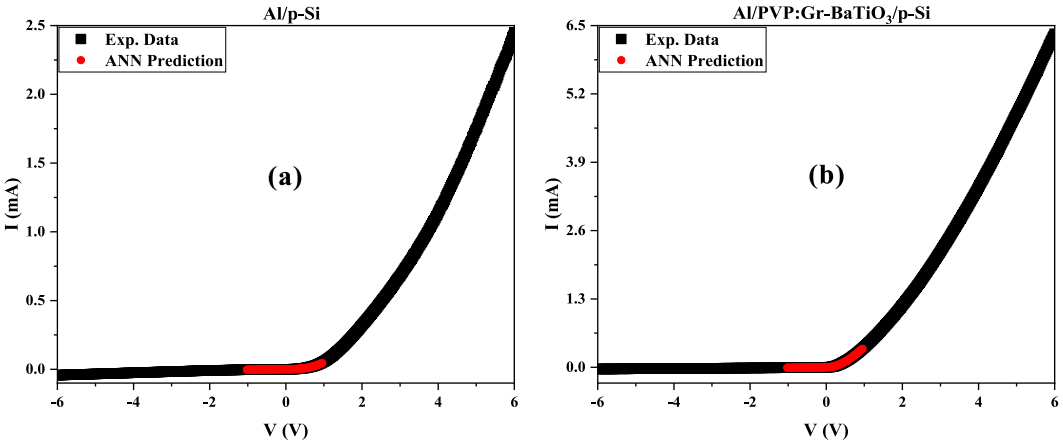

Fig. 7. The plots of I–V characteristics for the (a) MS- and (b) MPS-type SDs and their prediction with the ANN algorithm.

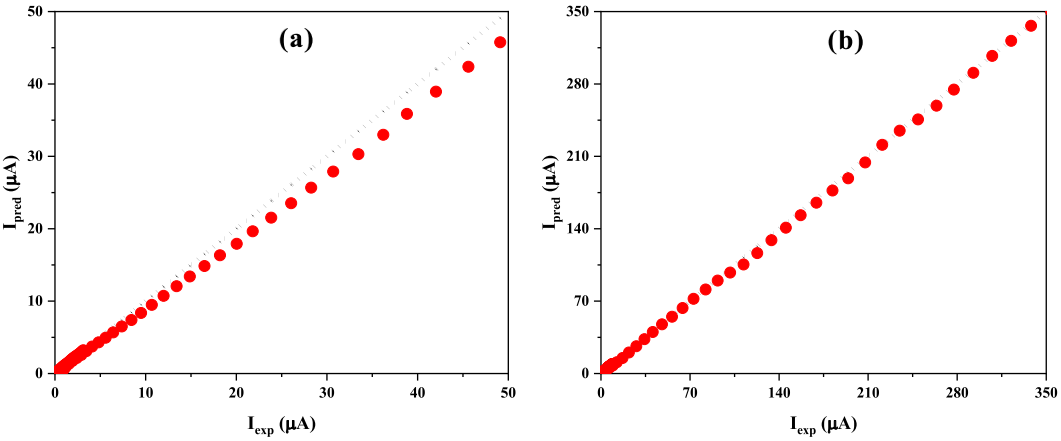

Fig. 8. The prediction amounts of the ANN model for the (a) MS- and (b) MPS-type SDs.

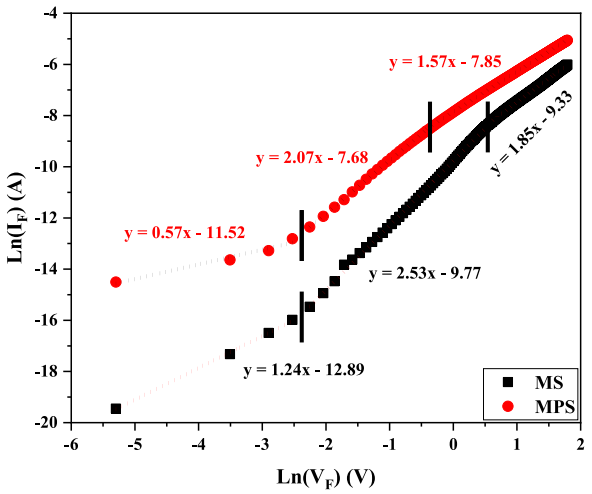

Fig. 9. The graph of $Ln(I_F)$-V_F for the MS and MPS configurations.

Table 2
The values (actual and prediction) of the slope of $Ln(I_F)$-V_F plots for different manufactured structures.

Slope		Actual	ANN
SD			
MS	**Part 1**	1.2430	1.0940
	Part 2	2.5277	2.6594
	Part 3	1.8507	1.8744
MPS	**Part 1**	0.5742	0.4678
	Part 2	2.0741	2.1511
	Part 3	1.5704	1.5908

slope anticipated by the ANN algorithm are also obtained (see Table 2). As seen, the ANN model is able to anticipate the CCMs into the prepared SDs well due to the small differences between the actual and predicted values. Because of the slope's closeness to unity, an ohmic behavior, or I ~ V, is seen at region I. Due to the low bias voltage in this part, minor charges from the electrodes are injected into the semiconductor [35]. Furthermore, at part II, the slope value is greater than two, and the current changes exponentially, that is, I ~ exp(V). The predominant CCM in this part is recombination-tunneling [36]. But, because of the distribution of traps formed by space-charge limited current (SCLC) at the band gap of the nanostructures used, the current exhibits a power behavior, or $I \sim V^m$. The SCLC transport mechanism is activated if the equilibrium charge concentration may be disregarded in favor of the injected electron concentration. It should be noted that increasing the number of electrons injected from the electrode causes the traps to fill up and the space charge to rise during the SCLC process [37].

In keeping with the CCMs investigation, Fig. 10 depicts the changes in Ln(I_R) as a function of $V_R^{0.5}$ for the MS and MPS configuration. Either the Poole-Frenkel (PF) or the Schottky emissions (SE) mechanisms are taken into consideration in order to analyze the CCMs into the MS and MPS SDs at the reverse bias voltage. If the PFE mechanism predominates, it allows us to define the I_R as [38],

$$I_R = I_0 \exp\left(\frac{\beta_{PF}}{kT}\sqrt{\frac{V}{d}}\right) \tag{8}$$

where I_0 is the leakage current, k is the Boltzmann constant, T is the temperature, β_{PF} is the field-lowering coefficient of Poole-Frenkel emission mechanism, V is the applied voltage, and d is the thickness of the interlayer. Moreover, if the SE process is the dominant mechanism into the SD, the I_R may be explained by the relationship below [39]:

$$I_R = AA^*T^2 \exp\left(-\frac{q\varphi_B}{kT}\right)\exp\left(\frac{\beta_{SE}}{kT}\sqrt{\frac{V}{d}}\right) \tag{9}$$

where A is a constant, A* refers to Richardson constant, φ_B is the potential barrier height, and β_{SE} the field lowering coefficient for the Schottky emission process. Typically, the β_{PF} value is two times of magnitude more than the β_{SE} value, which may be written as [38, 39]:

$$2\beta_{SE} = \beta_{PF} = \sqrt{\frac{q}{\pi\varepsilon_0\varepsilon_r}} \tag{10}$$

with ε_r being the permittivity of interlayer and q the electron charge. Fig. 10 presents the experimental changes of Ln(I_R) in terms of $V_R^{0.5}$ for the MS and MPS SDs. A linear portion is appeared in these graphs, as is evident. Therefore, the slope of these linear components equals the field lowering coefficient value, which for MPS and MS diodes was determined and represented in Table 3. Furthermore, the value of the β_{PF} coefficient for the MS and MPS configurations are anticipated by the ANN algorithm used in this work (see Table 3).

In order to determine the CCM into the MS and MPS structures at the reverse bias, the experimental values of the β_{PF} should be compared with the theoretical ones. The theoretical findings of β_{PF} for the MS and MPS SDs prepared in this research are computed and introduced in Table 3. It is observed that in the reverse bias region, the SE mechanism predominates for the MPS SD and the PFE mechanism for the MS structure. It is necessary to note that the value of β_{PF} predicted by the ANN model is very close to the actual values, indicating that the ANN can appropriately predict the CCM in the MS and MPS structures at the reverse bias.

4.5. ANN prediction of electronic parameters

At voltages in the forward bias region and by assuming a R_s and the voltages higher than 3kT/q, the I–V relationship in an SD at room temperature could be given by Ref. [40];

$$I = I_0\left[\exp\left(\frac{q(V - IR_s)}{nkT}\right) - 1\right], \tag{11}$$

where q represents the electric charge, T is the temperature, and k is the Boltzmann constant. The value of I_0 is according to the linear portion of the ln(I)–V plot at zero-bias [41]:

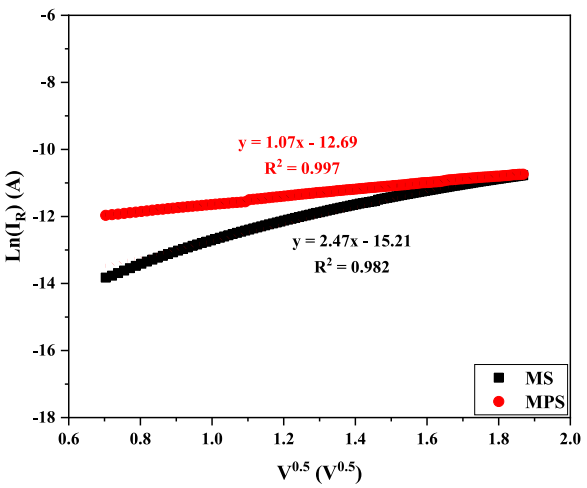

Fig. 10. The Ln(I_R)-$V_R^{0.5}$ plots of the MS and MPS samples.

$$I_0 = AA^*T^2 \exp\left(-\frac{q\varphi_{B0}}{kT}\right), \tag{12}$$

where other variables have clearly been established the literatures [40,41]. Table 4 presents the actual and prediction quantities of I_0 for the created SDs based on the ANN method. It is clear that the value of I_0 predicted by the ANN model is most closely matches the actual value. However, the PVP:Gr-$BaTiO_3$ nanocomposite leads to relatively increasing the leakage electronic current from 0.21 μA to 0.88 μA. In addition, a nanocomposite interlayer is mainly utilized to manage and control the height of potential barrier in the MS SD. Consequently, one of the essential electronic properties of SDs that must be obtained at zero-voltage is [42]:

$$\varphi_{B0} = \frac{kT}{q}\ln\left(\frac{AA^*T^2}{I_0}\right). \tag{13}$$

The BHs of the acquired fabricated SDs are listed in Table 4. Moreover, ML technique has been used to predict the electronic current required to ascertain the BH of various SDs. In this instance, the actual value and the predictions of the ANN algorithm agree rather well. Physically, the BH of the MS junction has relatively decreased as soon as the PVP:Gr-$BaTiO_3$ interlayer is positioned at the M/S interface.

The ideality factor, which determines an SD's behavior with respect to the ideality diode, is one of the crucial electronic characteristics of SDs that this study examines. The quantity of native/deposited interfacial layer, which includes ferroelectric, insulator, and polymer materials, at the M/S contact is unity in an ideal situation but usually differs from that. Other significant factors that impact the ideality factor are the density of interface/surface states generated at the interface between the interlayer and semiconductor, the interlayer thickness and dielectric quantity, and the depletion layer thickness, which is determined by the dopant content of donor/acceptor atomic elements in the pure semiconductor. The ideality factor is often indicated by the slope of the Ln(I)–V profile as [43]:

$$n = \frac{q}{kT}\left(\frac{dV}{d(lnI)}\right). \tag{14}$$

It is important to note that additional processes that affect the ideality factor and CTMs/CCMs occurred into the MPS SDs include electron tunnelling through the potential barrier with interface states, e^--h^+ pair creation and recombination, and barrier reduction as a result of image-force effect [1,44]. Table 4 displays the computed value of n for the built SDs in absence/presence of an interlayer at the M/S interface. Its drop from 4.60 for MS to 2.70 for MPS indicates that the presence of the PVP:Gr-$BaTiO_3$ nanocomposite interlayer brings the SD behavior closer to the ideal scenario.

One more time, the ANN algorithm has predicted the n amount for the taken-into-consideration SDs. It is evident that the ANN model determines the ideality coefficient of fabricated SDs with outstanding precision and low deviation.

Series resistance (R_s) is one electric characteristic of diodes that affects the rectifying ratio (RR) and hence the efficacy of SDs. Some of the sources from which it originated are the probe wires, the rectifier/ohmic junctions deposited on the front and back of the semiconductor layer, the semiconductor resistance, the non-uniform distribution of the donor/acceptor atomic elements doped into the semiconductor, and the residual contaminants from the cleaning procedure among the junctions [45,46]. Although the R_s may be ignored at the depletion and inversion zones, it will perform better at the accumulation zone [1,2]. In this study, R_s and R_{sh} are calculated using the ohmic law, which is expressed as;

$$R_i = \frac{dV_i}{dI_i}. \tag{15}$$

The amount of R_s acquired for the manufactured SDs without/with the PVP:Gr-$BaTiO_3$ nanocomposite interlayer at +1 V is shown in Table 4. Additionally, the ANN technique is used to predict the value of series resistance of the taken-into-consideration SDs. As shown, there is a reasonable degree of agreement between the predictions made by ANN algorithm and the actual values.

As can be seen in Table 4, the value of ideality factor is greater than unity, especially for MS type Schottky structure. On the other hand its value is much comparatively lower for MPS due to the passivation effect of the PVP:Gr-$BaTiO_3$ nanocomposite interlayer. It is well known that the value of ideality factor (n) should be unity in the ideal case. However, it considerably deviates from unity in applications according to $n = 1 + d_i/\varepsilon_i\,[\varepsilon_s/W_d + qN_{ss}]$. Because its value depends on various factors such as the existence of native or deposited interfacial layer between metal and semiconductor, the presence of surface states located between interfacial layer and semiconductor, doping concentration of donor (N_d) or acceptor (N_a) atoms, and depletion layer width ($W_d = [(2\varepsilon_s\varepsilon_0 V_{bi})/qN_a]$) [45]. In these relations, the quantities of ε_s, ε_i, ε_0, d_i, V_{bi} are the permittivity of the semiconductor, the permittivity of the interfacial layer, the permittivity of free space, thickness of the interfacial layer, and built-in voltage, respectively. The other reason of high value of ideality factor is the barrier inhomogeneity between metal and semiconductor [45]. The electrons which don't have enough energy to pass over the mean barrier height, can pass through these patches or lower barriers, leading to an increase in the current or ideality factor. Based

Table 3
The experimental, theoretical, and prediction values of β for different samples.

B_{PF} ($eV^{-1}.cm^{-2}$)	Exp.	Theory	ANN
SD			
MS	4.98×10^{-5}	3.66×10^{-5}	5.02×10^{-5}
MPS	8.76×10^{-6}	1.52×10^{-5}	8.51×10^{-6}

Table 4
The actual and prediction amounts of electronic parameters for the manufactured SDs.

Val	Actual						ANN					
SD	I_0 (μA)	Φ_{B0} (eV)	n	R_s (kΩ)	R_{sh} (MΩ)	RR	I_0 (μA)	Φ_{B0} (eV)	n	R_s (kΩ)	R_{sh} (MΩ)	RR
MS	0.21	0.74	4.60	19.42	0.12	59	0.12	0.76	4.52	20.85	0.11	53
MPS	0.88	0.71	2.70	2.70	0.33	120	1.04	0.70	2.80	2.72	0.32	116

on the equation (11) which defines the I–V relation for a Schottky structure, the parameter of n(V) is derived as $n(V) = qV/kTln(I/I_0)$. In these equations, the quantity of I_0 is the reverse saturation current at zero bias. As can be clearly seen in these equations, the value of n also changes with voltage and current [46].

It is noteworthy that the causes of the shunt resistance (R_{sh}) at the reverse bias voltage are phenomena such contaminants at the contact area, probing wire-ground patches, and leakage electronic current across the interlayer [47]. Furthermore, for large enough forward bias voltages, the Ln(I)–V plot will diverge from the linearity form because the applied voltage (V_a) is contributed throughout the MPS configuration with R_s and N_{ss}, given $V_a = V_i + V_{Rs} + V_d + V_{ss}$ [48]. Table 4 introduces the value of R_{sh}, examined at room temperature and a reverse bias voltage of −1 V, for the generated SDs with/without the PVP:Gr-$BaTiO_3$ interlayer. The presence of the PVP:Gr-$BaTiO_3$ nanocomposite relatively rises the shunt resistance of the MS SD. In order to contrast with the actual quantities, the amount of R_{sh} has been calculated using the ANN technique. The ANN model has anticipated the R_{sh} value with the least amount of deviation from the actual amounts. The ANN predictions of the R_{sh} quantities for the investigated SDs are nearest to the actual values.

Besides, the rectifying rate of the MS and MPS SDs is characterized by the RR parameter, which may be described as the ratio of the electronic current at the forward voltage (+1 V) to the reverse voltage (−1 V) as $RR=I_F/I_R$ [49]. Table 4 provides the RR quantity of the manufactured SDs utilized in this study at ambient temperature. It is demonstrated that the RR of the MS SD would significantly be better by placing the PVP:Gr-$BaTiO_3$ nanocomposite interlayer at the M/S contact. Since the ANN algorithm has predicted the electronic current of the fabricated SDs at a voltage range from -1V to +1V, the electric currents predicted by the ANN at the reverse and forward bias regions may be used to determine the RR amounts of various SDs. The RR quantities predicted with the ANN model show the best level of agreement between the predicted and actual amounts.

Notably, the deviation of the SD from ideal behavior may be attributed to two factors: the non-uniform distribution of the metallic and metal-oxide elements doped into the semiconductor and the surface/interface states. By considering N_{ss}'s dependence on voltage applied at equilibrium condition, the defect's relevance may be understood by using the following relation [50–52]:

$$N_{ss}(V) = \frac{1}{q}\left[\frac{\varepsilon_i}{\delta}(n(V)-1) - \frac{\varepsilon_s}{W_D}\right], \tag{16}$$

where δ is the interlayer thick (~100 nm) and W_D is the width of the depletion layer. Furthermore, the permittivity of the semiconductor and interfacial layers is indicated by ε_s and ε_i, respectively. It should be noted that the following expression represents the energy difference between the valance band and N_{ss} level of a p-type semiconductor [53]:

$$E_{ss} - E_v = q(\Phi_e - V). \tag{17}$$

Considering the relationship between Φ_e, R_s, and n(V), the following might be produced [53]:

$$\Phi_e - \Phi_{B0} = \left(1 - \frac{1}{n(V)}\right)V. \tag{18}$$

Eqs. (16)–(18) may be used to get the N_{ss} values for the prepared SDs shown in Table 5. It is clear that the density of interface states is decreased when a nanocomposite interfacial layer forms between the semiconductor and the metal. This is because the surface of the semiconductor layer becomes passivated as a result of the nanocomposite interlayer [46]. Note that the production of potential BH, native/deposited interlayer at the M/S interface, surface-states density (N_{ss}) and their uniform distribution are the causes of the transport/conduction processes (CTs/CMs) into the SDs [50–54]. Furthermore, the ANN technique is used to anticipate the N_{ss} amount for the provided SDs. The predictions of the ANN algorithm show high agreement with the actual values for both MS and MPS SDs.

5. Conclusions

In this paper, two SDs with the designs of Al/p-Si (MS) and Al/PVP:GR-$BaTiO_3$/p-Si (MPS) were built in order to investigate the effects of the nanocomposite interlayer on the CCMs and the basic electronic characteristics of the MS SD. Then, the I–V characteristics of the SDs were measured to determine the CCMs at the forward/reverse bias and the TE theory was employed to calculate their main

Table 5
The actual and prediction quantities of N_{ss} for the fabricated SDs.

$N_{ss} \times 10^{13}$ (eV^1 cm^{-2})	Actual	ANN
SD		
MS	9.4830	9.4427
MPS	1.8642	1.8139

electric factors, i.e., I_0, Φ_{B0}, n, R_s, R_{sh}, RR, and N_{ss}. The CCMs and all of the previously listed electronic factors have been predicted using ANN technique and compared with the experimental results. By computing the slopes of the different parts of the $Ln(I_F)$-V_F profiles for the MS and MPS structures, it was found that there are different mechanisms occurred into these structures due to the ohmic, exponential, and power behaviors. At the reverse bias region, the field-lowering coefficient of the prepared structures were obtained, indicating that the SE mechanism predominates into the MS configuration whereas the PFE process is the dominant CCM into the MPS structure because of inserting the PVP:Gr-$BaTiO_3$ nanocomposite between the semiconductor and metal layers.

The acquired findings reveal that the electrical variables of R_s and N_{ss} for MS SD declines and the values of R_{sh} and RR increases when the PVP:Gr-$BaTiO_3$ interlayer is utilized. Moreover, the I_0 of the MS contact slightly raises and the BH value relatively declines when the PVP:Gr-$BaTiO_3$ nanocomposite interlayer is positioned in the M/S interface. When the interfacial nanocomposite layer lowers the n value from 4.60 for MS SD to 2.70 for MPS SD, the conduct of the MS configuration approaches the ideal state. Furthermore, the RR of the MS SD would significantly be better by the addition of an interfacial nanocomposite layer amidst the semiconductor and metal layers. The interface states density of the MPS structure decreases when the PVP:Gr-$BaTiO_3$ layer interposes itself between the metal and semiconductor. Consequently, the efficacy of the MS-type SD is greatly improved by the PVP polymer-doped Gr and $BaTiO_3$ nanoparticles.

Due to the experimental and prediction values of the slopes at the forward bias region and the β_{PF} coefficient at the reverse bias voltages, the ANN algorithm is a suitable method to anticipate the CCMs occurred into the MS and MPS SDs at the forward/reverse bias regions. Moreover, the ANN was able to predict the basic electronic variables of the MS and MPS SDs after training with 400 data points. The values of the electronic variables, i.e., I_0, Φ_{B0}, n, R_s/R_{sh}, RR, and N_{ss}, of the fabricated MS and MPS SDs were predicted by the ANN with high accuracy and slightest deviation from the actual results. Because of the MSE values, the ANN model' predicting performance for the SDs electronic current is dependable. Consequently, this study can offer valuable perspectives for further research endeavors that seek to identify alternative, more fitting algorithms and maximize their refinement and optimization.

Funding statement

Not applicable.

CRediT authorship contribution statement

Yashar Azizian-Kalandaragh: Writing – review & editing, Supervision, Project administration, Methodology, Conceptualization. **Süleyman Özçelik:** Writing – review & editing, Supervision. **Ali Barkhordari:** Writing – original draft, Software, Investigation, Formal analysis, Data curation, Conceptualization. **Şemsettin Altındal:** Writing – review & editing, Supervision.

Declaration of competing interest

The authors declare that they have no known competing financial interests or personal relationships that could have appeared to influence the work reported in this paper.

Data availability

Data will be made available on request.

References

[1] S.M. Sze, K.K. Ng, LEDs and lasers, Physics of Semiconductor Devices 3 (2006) 601–657.
[2] E.H. Nicollian, J.R. Brews, MOS (metal oxide semiconductor), Phys. Technol. (1982) 920.
[3] H.C. Card, E.H. Rhoderick, Studies of tunnel MOS diodes I. Interface effects in silicon Schottky diodes, J. Phys. Appl. Phys. 4 (10) (1971 Oct 1) 1589.
[4] R.T. Tung, The physics and chemistry of the Schottky barrier height, Appl. Phys. Rev. 1 (1) (2014 Mar 13) 011304.
[5] N.A. Al-Ahmadi, Metal oxide semiconductor-based Schottky diodes: a review of recent advances, Mater. Res. Express 7 (3) (2020 Mar 9) 032001.
[6] Ş. Altındal, A. Barkhordari, Y. Azizian-Kalandaragh, B.S. Çevrimli, H.R. Mashayekhi, Dielectric properties and negative-capacitance/dielectric in Au/n-Si structures with PVC and (PVC: Sm2O3) interlayer, Mater. Sci. Semicond. Process. 147 (2022 Aug 15) 106754.
[7] M.H. Al-Dharob, H.E. Lapa, A. Kökce, A.F. Özdemir, D.A. Aldemir, Ş. Altındal, The investigation of current-conduction mechanisms (CCMs) in Au/(0.07 Zn-PVA)/n-4H-SiC (MPS) Schottky diodes (SDs) by using (IVT) measurements, Mater. Sci. Semicond. Process. 85 (2018 Oct 1) 98–105.
[8] S. Altındal Yerişkin, M. Balbaşı, İ. Orak, The effects of (graphene doped-PVA) interlayer on the determinative electrical parameters of the Au/n-Si (MS) structures at room temperature, J. Mater. Sci. Mater. Electron. 28 (18) (2017 Sep) 14040–14048.
[9] O. Çiçek, Ş. Altındal, Y. Azizian-Kalandaragh, A highly sensitive temperature sensor based on Au/graphene-PVP/n-Si type Schottky diodes and the possible conduction mechanisms in the wide range temperatures, IEEE Sensor. J. 20 (23) (2020 Jul 15) 14081–14089.
[10] V.R. Reddy, C.V. Prasad, Surface chemical states, electrical and carrier transport properties of Au/ZrO2/n-GaN MIS junction with a high-k ZrO2 as an insulating layer, Mater. Sci. Eng., B 231 (2018 May 1) 74–80.
[11] G. Ersöz, İ. Yücedağ, Y. Azizian-Kalandaragh, I. Orak, Ş. Altındal, Investigation of electrical characteristics in Al/CdS-PVA/p-Si (MPS) structures using impedance spectroscopy method, IEEE Trans. Electron. Dev. 63 (7) (2016 May 24) 2948–2955.
[12] Y. Azizian-Kalandaragh, Dielectric properties of CdS-PVA nanocomposites prepared by ultrasound-assisted method, Optoelectron Adv Mater Rapid Commun 4 (11) (2010 Nov 10) 1655–1658.
[13] E.H. Houssein, Z. Abohashima, M. Elhoseny, W.M. Mohamed, Machine learning in the quantum realm: the state-of-the-art, challenges, and future vision, Expert Syst. Appl. 21 (2022 Jan) 116512.
[14] K. Crampon, A. Giorkallos, M. Deldossi, S. Baud, L.A. Steffenel, Machine-learning methods for ligand–protein molecular docking, Drug Discov. Today 27 (1) (2022 Jan 1) 151–164.

[15] B. Mueller, T. Kinoshita, A. Peebles, M.A. Graber, S. Lee, Artificial intelligence and machine learning in emergency medicine: a narrative review, Acute medicine & surgery 9 (1) (2022 Jan) e740.
[16] O. Ivanciuc, Applications of support vector machines in chemistry, Rev. Comput. Chem. 23 (2007 Jan 25) 291.
[17] H. Doğan, S. Duman, Y. Torun, S. Akkoyun, S. Doğan, U. Atici, Neural network estimations of annealed and non-annealed Schottky diode characteristics at wide temperatures range, Mater. Sci. Semicond. Process. 149 (2022 Oct 1) 106854.
[18] T. Güzel, A.B. Çolak, Investigation of the usability of machine learning algorithms in determining the specific electrical parameters of Schottky diodes, Mater. Today Commun. 33 (2022 Dec 1) 104175.
[19] Y. Torun, H. Doğan, Modeling of Schottky diode characteristic by machine learning techniques based on experimental data with wide temperature range, Superlattice. Microst. 160 (2021 Dec 1) 107062.
[20] H.A. Ali, E.F. El-Zaidia, R.A. Mohamed, Experimental investigation and modeling of electrical properties for phenol red thin film deposited on silicon using back propagation artificial neural network, Chin. J. Phys. 67 (2020 Oct 1) 602–614.
[21] T. Güzel, A.B. Çolak, Artificial intelligence approach on predicting current values of polymer interface Schottky diode based on temperature and voltage: an experimental study, Superlattice. Microst. 153 (2021 May 1) 106864.
[22] H.T. Kim, S. Nahm, J.D. Byun, Y. Kim, Low-fired (Zn, Mg) TiO3 microwave dielectrics, J. Am. Ceram. Soc. 82 (12) (1999 Dec) 3476–3480.
[23] Y. Gui, S. Li, J. Xu, C. Li, Study on TiO2-doped ZnO thick film gas sensors enhanced by UV light at room temperature, Microelectron. J. 39 (9) (2008 Sep 1) 1120–1125.
[24] Z. Durmus, A. Durmus, H. Kavas, Synthesis and characterization of structural and magnetic properties of graphene/hard ferrite nanocomposites as microwave-absorbing material, J. Mater. Sci. 50 (2015 Feb) 1201–1213.
[25] A. Barkhordari, S. Özçelik, Ş. Altındal, G. Pirgholi-Givi, H. Mashayekhi, Y. Azizian-Kalandaragh, The effect of PVP: BaTiO3 interlayer on the conduction mechanism and electrical properties at MPS structures, Phys. Scripta 96 (8) (2021 May 26) 085805.
[26] E. Ahmadloo, S. Azizi, Prediction of thermal conductivity of various nanofluids using artificial neural network, Int. Commun. Heat Mass Tran. 74 (2016 May 1) 69–75.
[27] M. Awad, R. Khanna, Efficient Learning Machines: Theories, Concepts, and Applications for Engineers and System Designers, Springer nature, 2015.
[28] M. Rupp, A. Tkatchenko, K.R. Müller, O.A. Von Lilienfeld, Fast and accurate modeling of molecular atomization energies with machine learning, Phys. Rev. Lett. 108 (5) (2012 Jan 31) 058301.
[29] A. Ali, A. Abdulrahman, S. Garg, K. Maqsood, G. Murshid, Application of artificial neural networks (ANN) for vapor-liquid-solid equilibrium prediction for CH4-CO2 binary mixture, Greenhouse Gases: Sci. Technol. 9 (1) (2019 Feb) 67–78.
[30] A.B. Çolak, O. Yıldız, M. Bayrak, B.S. Tezekici, Experimental study for predicting the specific heat of water based Cu-Al2O3 hybrid nanofluid using artificial neural network and proposing new correlation, Int. J. Energy Res. 44 (9) (2020 Jul) 7198–7215.
[31] S. Öcal, M. Gökçek, A.B. Çolak, M. Korkanç, A comprehensive and comparative experimental analysis on thermal conductivity of TiO 2-CaCO 3/Water hybrid nanofluid: proposing new correlation and artificial neural network optimization, Heat Tran. Res. 52 (17) (2021).
[32] S. Parhoodeh, M. Kowsari, Synthesis, characterization and study of band gap variations of vanadium doped indium oxide nanoparticles, Phys. B Condens. Matter 498 (2016 Oct 1) 27–32.
[33] G. Pirgholi-Givi, Y. Azizian-Kalandaragh, J. Farazin, Comparison of the photocatalytic activity of perovskite structures: bismuth, barium, and zinc titanate nanostructures for photodegradation of methylene blue from water, J. Photochem. Photobiol. Chem. 408 (2021 Mar 1) 113104.
[34] K. Potje-Kamloth, Chemical gas sensors based on organic semiconductor polypyrrole, Crit. Rev. Anal. Chem. 32 (2) (2002 Apr 1) 121–140.
[35] M. Gökçen, T. Tunç, Ş. Altındal, I. Uslu, Electrical and photocurrent characteristics of Au/PVA (Co-doped)/n-Si photoconductive diodes, Mater. Sci. Eng. B 177 (5) (2012 Mar 25) 416–420.
[36] A. Tataröl u, A.A. Hendi, R.H. Alorainy, F. Yakuphanöl u, A new aluminum iron oxide Schottky photodiode designed via sol—gel coating method, Chin. Phys. B 23 (5) (2014 Mar 25) 057504.
[37] A. Buyukbas-Uluşan, S.A. Yerişkin, A.D. Tataroğlu, M. Balbaşı, Y.A. Kalandaragh, Electrical and impedance properties of MPS structure based on (Cu 2 O–CuO–PVA) interfacial layer, J. Mater. Sci. Mater. Electron. 29 (2018 May) 8234–8243.
[38] V.R. Reddy, V. Manjunath, V. Janardhanam, Y.H. Kil, C.J. Choi, Electrical properties and current transport mechanisms of the Au/n-GaN Schottky structure with solution-processed high-k BaTiO3 interlayer, J. Electron. Mater. 43 (9) (2014 Sep 1) 3499–3507.
[39] H. Schroeder, Poole-Frenkel-effect as dominating current mechanism in thin oxide films—an illusion? J. Appl. Phys. 117 (21) (2015 Jun 7).
[40] Z. Durmus, A. Durmus, H. Kavas, Synthesis and characterization of structural and magnetic properties of graphene/hard ferrite nanocomposites as microwave-absorbing material, J. Mater. Sci. 50 (3) (2015 Feb) 1201–1213.
[41] A. Barkhordari, Ş. Altındal, G. Pirgholi-Givi, H. Mashayekhi, S. Özçelik, Y. Azizian-Kalandaragh, The influence of PVC and (PVC: SnS) interfacial polymer layers on the electric and dielectric properties of Au/n-Si structure, Silicon 15 (2022 Aug), 1-1.
[42] Ş. Altındal, Ö. Sevgili, Y. Azizian-Kalandaragh, A comparison of electrical parameters of Au/n-Si and Au/(CoSO4–PVP)/n-Si structures (SBDs) to determine the effect of (CoSO4–PVP) organic interlayer at room temperature, J. Mater. Sci. Mater. Electron. 30 (10) (2019 May) 9273–9280.
[43] O. Vargas, Á. Caballero, J. Morales, Enhanced electrochemical performance of maghemite/graphene nanosheets composite as electrode in half and full Li–ion cells, Electrochim. Acta 130 (2014 Jun 1) 551–558.
[44] Ş. Altındal, A. Barkhordari, S. Özçelik, G. Pirgholi-Givi, H.R. Mashayekhi, Y. Azizian-Kalandaragh, A comparison of electrical characteristics of Au/n-Si (MS) structures with PVC and (PVC: Sm2O3) polymer interlayer, Phys. Scripta 96 (12) (2021 Oct 19) 125838.
[45] R. Ashiri, A. Nemati, M.S. Ghamsari, S. Sanjabi, M. Aalipour, A modified method for barium titanate nanoparticles synthesis, Mater. Res. Bull. 46 (12) (2011 Dec 1) 2291–2295.
[46] A. Barkhordari, S. Özçelik, Ş. Altındal, G. Pirgholi-Givi, H. Mashayekhi, Y. Azizian-Kalandaragh, The effect of PVP: $BaTiO_3$ interlayer on the conduction mechanism and electrical properties at MPS structures, Phys. Scripta 96 (8) (2021 May 26) 085805.
[47] J. Ansaree, S. Upadhyay, Thermal analysis of formation of nano-crystalline BaTiO3 using Ba(NO3)2 and TiO2, Processing and Application of Ceramics 9 (4) (2015) 181–185.
[48] P. Yu, B. Cui, Q. Shi, Preparation and characterization of BaTiO3 powders and ceramics by sol-gel process using oleic acid as surfactant, Mater. Sci. Eng., A 473 (1–2) (2008 Jan 25) 34–41.
[49] Ş. Altındal, A. Barkhordari, G. Pirgholi-Givi, M. Ulusoy, H. Mashayekhi, S. Özçelik, Y. Azizian-Kalandaragh, Comparison of the electrical and impedance properties of Au/(ZnOMn: PVP)/n-Si (MPS) type Schottky-diodes (SDs) before and after gamma-irradiation, Phys. Scripta 96 (12) (2021 Dec 30) 125881.
[50] N. Rahman, M. Husain, J. Yang, M. Sajjad, G. Murtaza, M. Ul Haq, A. Habib, A. Rauf, A. Karim, M. Nisar, M. Yaqoob, First principle study of structural, electronic, optical and mechanical properties of cubic fluoro-perovskites:(CdXF3, X= Y, Bi), The European Physical Journal Plus 136 (3) (2021 Mar), 1-1.
[51] M. Husain, N. Rahman, R. Khan, S. Zulfiqar, S.A. Khattak, S.N. Khan, M. Sohail, A. Iqbal, A.H. Reshak, A. Khan, Structural, electronic, elastic, and magnetic properties of NaQF3 (Q= ag, Pb, Rh, and Ru) flouroperovskites: a first-principle outcomes, Int. J. Energy Res. 46 (3) (2022 Mar 10) 2446–2453.
[52] M. Husain, N. Rahman, R. Khan, M. Sohail, A.A. Khan, H.O. Elansary, T.K. El-Abedin, E.A. Mahmoud, S.A. Abdelmohsen, A. Khan, Exploring the exemplary structural, electronic, optical, and elastic nature of inorganic ternary cubic XBaF3 (X= Al and Tl) employing the accurate TB-mBJ approach, Semicond. Sci. Technol. 37 (7) (2022 May 18) 075004.
[53] J. Saddique, M. Husain, N. Rahman, R. Khan, A. Iqbal, M. Sohail, S.A. Khattak, S.N. Khan, A.A. Khan, A.H. Reshak, A. Khan, Modeling structural, elastic, electronic and optical properties of ternary cubic barium based fluoroperovskites MBaF3 (M= Ga and In) compounds based on DFT, Mater. Sci. Semicond. Process. 139 (2022 Mar 1) 106345.
[54] M. Husain, N. Rahman, H. Albalawi, S. Ezzine, M. Amami, T. Zaman, A.U. Rehman, M. Sohail, R. Khan, A.A. Khan, A. Khan, Examining computationally the structural, elastic, optical, and electronic properties of CaQCl 3 (Q= Li and K) chloroperovskites using DFT framework, RSC advances 12 (50) (2022) 32338–32349.